Combined first-principles and electromagnetic simulation study of *n*-type doped anatase TiO_2 for the applications in infrared surface plasmon photonics

Thien Duc Ngo,[1,2] Thang Duy Dao,[1] Nguyen Thanh Cuong,[3] Naoto Umezawa,[1,4] and Tadaaki Nagao[1,2,*]

[1]*International Center for Materials Nanoarchitectonics (MANA), National Institute for Materials Science (NIMS), 1-1 Namiki, Tsukuba, Ibaraki 305-0044, Japan*

[2]*Department of Condensed Matter Physics, Graduate School of Science, Hokkaido University, Kita 10, Nishi 8, Kita-ku, Sapporo 060-0810, Japan*

[3]*International Center for Young Scientists, National Institute for Materials Science, 1-1 Namiki, Tsukuba, Ibaraki 305-0044, Japan*

[4]*Semiconductor R&D Center, Samsung Electronics, 1, Samsungjeonja-ro, Hwaseong-si, Gyeonggi-do 18448, South Korea*

(Received 23 June 2019; revised manuscript received 10 December 2019; accepted 25 March 2020; published 7 May 2020)

We investigated the electronic structures and optical properties of doped anatase TiO_2 in the infrared region using first-principles density functional theory with the independent-particle approximation. By examining the dopants from groups V-B, VI-B, and VII-A of the Periodic Table of Elements, we found that the anatase TiO_2 doped with different dopants Nb, Ta, W, and F showed excellent plasmonic properties in the near-infrared region with nonmetal-to-metal crossover frequencies within a range of 2.0–2.7 μm along the densest-plasma direction. Furthermore, we discussed the prospect of producing low-cost robust mid- to far-infrared plasmonic devices based on doped anatase TiO_2. Our combined analysis with electromagnetic numerical simulation showed that the doped anatase TiO_2 exhibited well-defined surface plasmon polariton as well as localized surface plasmon resonances in the midinfrared region. We expect that this *n*-type doped anatase TiO_2 is a highly promising material for infrared plasmonic applications in harsh environments such as aqueous solutions and/or high temperature.

DOI: 10.1103/PhysRevMaterials.4.055201

I. INTRODUCTION

In general, many metals exhibit plasmons and their surface mode (surface plasmons) to a certain degree, which serves as the foundation for various nanophotonics applications such as optical waveguides, photovoltaics, thermophotovoltaics, and photocatalysis [1–3]. However, most metals tend to be oxidized and corroded rapidly, which will deteriorate their properties in harsh conditions such as in high temperature and humid environments as well as in aqueous solutions. An exception is Au, which is chemically stable and inert, which means that its physical properties do not alter significantly even in severe environments. However, Au is a noble metal and always suffers from its high price and its low mechanical strength, especially at high temperatures. Many efforts have been made in the past decade to search for high-performance, and yet robust, practical plasmonic materials, particularly plasmonic transparent conductive oxides (TCOs), in order to explore their unique properties, which are not possible in conventional elemental metals [4]. For example, tin-doped indium oxide (ITO), aluminum-doped zinc oxide (AZO), gallium-doped zinc oxide (GZO), or indium-doped zinc oxide can support plasmons [4–6], and their generic applications, such as thin-film solar cells, low-emissivity (low-*E*) windows [7], and organic light-emitting diodes (OLED) [8], have attracted much interest. The most significant advantage of doped semiconductors is that their optical properties (e.g., plasma frequencies) can be controlled by varying the carrier concentration. However, these conventional TCOs are known to be corrosive in solution and optically unstable at high temperatures [9], which make them unsuitable for use in tough conditions such as in photocatalysis and in thermal emitter applications.

Titanium dioxide (TiO_2) is a low-cost transparent oxide that exhibits excellent chemical/thermal stability, as well as catalytic surface activity [10,11], which make it widely utilized in industry such as self-cleaning window/wall coating, water-repellent paints, pigment, sunscreen, as well as electrodes for dye-sensitized solar cells. In this context, TiO_2-based TCOs have gained much attention from the scientific community in relation to the application in transparent electrodes for flat panel displays (FPDs) and solar cells. However, to the best of our knowledge, applications for plasmonic devices have not been studied.

To exploit the benefits of TiO_2 as an effective material for nanophotonics, by taking full advantage of TiO_2 as a plasmonic material, it is crucial for TiO_2 to exhibit metallic behavior at the targeted wavelengths. Doping is generally considered as the fundamental approach to convert semiconducting TiO_2 into metallic conductors. Regarding the theoretical prediction for doped TiO_2 as TCO, first-principles density functional theory (DFT) with a hybrid functional was

*Author to whom all correspondence should be addressed: nagao.tadaaki@nims.go.jp

used to predict the conductive properties of doped anatase and rutile TiO_2, and the results showed that doped anatase TiO_2 was metallic, and doped rutile TiO_2 was semiconducting [12]. Recent experiments [13–16] revealed that Nb-doped TiO_2, F-doped TiO_2, and W-doped TiO_2 films had high carrier density and unique electrical and optical properties. Since most studies of doped TiO_2 have focused on visible transparency and high dc conductivity in relation to the FPD and photovoltaic applications, there is a paucity of studies on the application of doped TiO_2 for infrared (IR) plasmonics. In addition, there has been no systematic theoretical study on the effects of doping on the electronic structures and optical properties of anatase TiO_2 in the IR region. It is quite essential to investigate the effect of carrier concentration on the optical permittivity of doped semiconductors in order to determine the tunability of the optical properties of this unique class of plasmonic materials.

In principle, the optical response is expected to be precisely obtained by adopting the quasiparticle effect (*GW* approximation), the spin-orbit-coupling effect, electron-phonon scattering, and the local-field effect. Recently, several studies have used fully first-principles calculations to compute electron-phonon scattering in different plasmonic materials, including noble metals, transition metals, and two-dimensional (2D) materials [17–22]. However, these calculations require high-level approaches such as the *GW* approximation and the Bethe-Salpeter equation (BSE). In this study, since we need to adopt a large supercell (with 108 atoms) to simulate a doped anatase TiO_2, its computational expense becomes too high in such an approach to obtain results within a reasonable timescale. Therefore, we approach the problem here using a simpler model based on the independent-particle approximation (IPA) to balance the computational/time expense and accuracy. Because of the increasing demand to establish a combined theory-experiment approach for the development of various conductive ceramics, we chose a more practical and efficient approach with acceptable accuracy. Here, the IPA model is the simplest but most successful approach for simulating the optical response for many metallic systems [23–28]. In addition to the theoretical framework, it should be noted that there are several factors in real experiments that largely affect the optical response of the metallic systems in real experiments. For example, it is a well-known fact that nanoscale grain structures (surface nanomorphologies) of plasmonic materials can dramatically alter their optical response. A quantitative comparison of the experimental and theoretical results derived by a more sophisticated approach including electron-phonon coupling with the *GW* and BSE schemes is of great interest. But for such studies, elaborate experimental efforts are also needed to obtain atomically flat single-crystalline plasmonic films, which are rather challenging. Taking into account the current status of the crystal growth techniques and available materials, our IPA approach provides an adequate methodology and fruitful results to support the material developments in this field.

In this study, we investigated the electronic structures and optical properties of doped anatase TiO_2 in the IR region. We focus here on anatase TiO_2 rather than rutile TiO_2 due to the advantages of the former polymorph, such as lower effective mass [29,30] and higher mobility. In the first part of this article, by employing first-principles DFT and the IPA model, we studied the geometry, electronic structures, and optical properties of two types of doped anatase TiO_2: (i) $Ti_{1-x}M_xO_2$ (M = V, Nb, Ta, Cr, Mo, W) and (ii) $TiO_{2-x}F_x$ ($x = 0.03$). The objective of this part was to identify potential dopants for anatase TiO_2. In the latter part, we implemented electromagnetic simulations to investigate the performances of *n*-type doped TiO_2 by examining the surface plasmon polariton (SPP) at the doped TiO_2/air interface and the localized surface plasmon resonance (LSPR) of a doped TiO_2 nanocavity array in the IR region. The research approach presented in this work can also be applied for other TCO-based plasmonic materials and their potential applications in the IR region, such as infrared detectors, emitters, and infrared sensing devices [31–36].

II. COMPUTATIONAL METHOD

A. First-principles DFT simulations

The electronic structure and optical properties of undoped and doped anatase TiO_2 were calculated using DFT with the projector augmented wave (PAW) method [37], as implemented in the Vienna Ab initio Simulation Package (VASP) [38]. The Perdew-Burke-Ernzerhof (PBE) functional [39] within the generalized gradient approximation (GGA) was employed for the exchange-correlation potential. The plane-wave basis set with an energy cutoff of 520 eV was used for all simulations.

The anatase TiO_2 tetragonal crystal was simulated using a 108-atom 3×3×1 supercell consisting of 36 Ti and 72 O atoms, as shown in Fig. 1(a). We investigated doped anatase

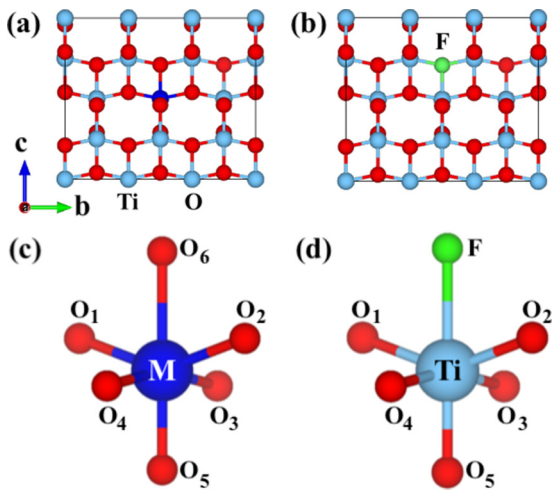

FIG. 1. (a) Local atomic structures of metal-doped anatase TiO_2 with a 108-atom 3 × 3 × 1 supercell extended from the conventional cell (hereafter: TiO_2:*M*, *M* = V,Cr,Nb,Mo,Ta,W). (b) Local atomic structure of the F-doped anatase TiO_2 (hereafter: TiO_2:F). (c) *M*-O bond length at the doping position. There are two types of O atom: equatorial *M*-O bonds (O_1, O_2, O_3, O_4) and apical *M*-O bonds (O_5, O_6). (d) Ti-F and Ti-O bond length in the case of TiO_2:F. The blue and red spheres represent the Ti and O atoms, respectively. The dark blue and green spheres represent the metals and F atoms, respectively. The structures shown here were visualized using visualization for electronic and structural analysis (VESTA) software [55].

TiO_2 (dopant concentration: 3%) by substituting 1 of the 36 Ti atoms in the supercell with a metal (M) atom from group VI-B (Cr, Mo, W) or group V-B (V, Nb, Ta) of the Periodic Table [Fig. 1(a)] and replacing one of the 72 O atoms with a F atom [Fig. 1(b)]. All of the atomic positions and volume were simultaneously relaxed until the residual force was less than 0.005 eV/Å. The structural optimization was conducted using a $3 \times 3 \times 3$ Monkhorst-Pack k-point mesh [40]. Both spin-polarized and non-spin-polarized calculations were performed to check the magnetic ordering of the doped anatase TiO_2 crystals. To compute the density of states (DOS), we used a dense $15 \times 15 \times 17$ Monkhorst-Pack k-point mesh. The electronic band structures and transport anisotropy of real doped system are perturbed by defects, impurities, or fluctuation of the chemical composition. Therefore, we employed the band-unfolding technique, as proposed by Popescu and Zunger [41]. The unfolding has been performed using the BandUP (Band Unfolding code for Plane-wave based calculations) [42,43] to conveniently compare the band structures of doped anatase supercells with the primitive cell. The HSE06 hybrid functional [44] with standard Hartree-Fock mixing ($\alpha = 0.25$) was also used to improve the electronic structure and band gap, and the results were compared with those obtained from experiments [45]. Because of the large computational cost, the optimized structures and spin-polarization effects obtained from the PBE functional were used in the supercell simulations using the HSE06 hybrid functional.

The frequency-dependent dielectric functions of doped anatase TiO_2 crystals were investigated using the IPA model [46]. The smearing width is set at 0.1 eV. We employed a $15 \times 15 \times 17$ Monkhorst-Pack k-point mesh with acceptable conduction bands to ensure convergence of the interband dielectric functions. If the doped anatase TiO_2 crystals showed metallic behavior, we calculated the interband and intraband electronic transitions [denoted by $\varepsilon^{\text{inter}}(\omega)$ and $\varepsilon^{\text{intra}}(\omega)$, respectively], which contributed to the total dielectric function $\varepsilon(\omega) = \varepsilon^{\text{inter}}(\omega) + \varepsilon^{\text{intra}}(\omega)$. The interband dielectric function is given by

$$\varepsilon^{\text{inter}}(\omega) = \varepsilon_1^{\text{inter}}(\omega) + i\varepsilon_2^{\text{inter}}(\omega). \tag{1}$$

The imaginary part of the interband dielectric function was determined using the following equation [46]:

$$\varepsilon_2^{\text{inter}}(\omega) = \frac{4\pi^2 e^2}{V} \lim_{q\to 0} \frac{1}{q^2} \sum_{c,v,\mathbf{k}} 2w_{\mathbf{k}} \delta(E_{c\mathbf{k}} - E_{v\mathbf{k}} - \omega) \times \langle u_{c\mathbf{k}+\mathbf{e}_\alpha q} | u_{v\mathbf{k}} \rangle \langle u_{v\mathbf{k}} | u_{c\mathbf{k}+\mathbf{e}_\beta q} \rangle, \tag{2}$$

where c and v denote the conduction- and valence-band states, respectively; $\mathbf{k}$, $w_{\mathbf{k}}$, and $E_{\mathbf{k}}$ denote the k-points, the weight of each k-point, and the single-electron energy state, respectively; $u_{c\mathbf{k}}$ represents the cell periodic part of the orbitals at the k-points $\mathbf{k}$; e and V represent the electron charge and cell volume, respectively; and $\mathbf{e}_\alpha$ and $\mathbf{e}_\beta$ represent the unit vectors in Cartesian space. Since anatase TiO_2 has a tetragonal structure, the dielectric functions along with the components xy, yz, and zx exhibit zero values, hence we only consider the optical properties along with the components xx, yy, and zz. Furthermore, we focus on the components that showed the highest plasma frequency (xx or yy, $\mathbf{E} \perp c$). See the Supplemental Material (Fig. S8) in Ref. [47] for the dielectric functions along the zz-component ($\mathbf{E} \parallel c$).

The real part of the interband dielectric function $\varepsilon_1^{\text{inter}}(\omega)$ was determined from the imaginary part $\varepsilon_2^{\text{inter}}(\omega)$ using the Kramers-Kronig relation [46]:

$$\varepsilon_1^{\text{inter}}(\omega) = 1 + \frac{2}{\pi} \text{P} \int_0^\infty \frac{\varepsilon_2^{\text{inter}}(\omega')\omega'}{\omega'^2 - \omega^2 + i\eta} d\omega', \tag{3}$$

where P is the principal value, and the complex shift η is an infinitesimal number used in Kramers-Kronig transformation.

The intraband dielectric function was obtained by using the Drude expression [48,49]:

$$\varepsilon^{\text{intra}}(\omega) = 1 - \frac{\omega_p^2}{\omega(\omega + i\gamma)}, \tag{4}$$

where ω_p is the plasma frequency and γ is the scattering rate.

See the Supplemental Material (Sec. S4) for details on the computational method used to calculate the plasma frequency and scattering rate [50–54].

B. Electromagnetic simulations

The optical spectra (transmittance, reflectance, and absorptivity) of the 1D plasmonic doped anatase TiO_2 structure were simulated using a 2D rigorous coupled-wave analysis (RCWA) (DiffractMOD, Synopsys' RSoft). For the electric field distribution, a 2D full-wave simulation based on the finite-difference time-domain (FDTD) method (FullWAVE, Synopsys' RSoft) was employed wherein periodic boundary conditions were used for both sides of the X direction. The perfectly matched layers were applied to both sides of the Z direction. For both RCWA and FDTD simulations, the excitation electromagnetic field propagated along the Z-axis and the electric field oscillated along the X-axis, the grid size was 2.5 nm, and the incident field amplitudes were normalized to 1.

III. RESULTS AND DISCUSSION

A. Crystal structures, electronic structure, and optical properties of *n*-type doped anatase TiO_2

In this section, we will first discuss the structural modulation of anatase TiO_2 under doping effects. Lattice parameters for a conventional cell of anatase determined using the PBE functional were $a = 3.805$ Å and $c = 9.725$ Å. Lattice parameters obtained using the hybrid functional were $a = 3.765$ Å and $c = 9.629$ Å, which showed very good agreement with those in previous studies ($a = 3.766$ Å, $c = 9.637$ Å) [12,56] and experiments ($a = 3.782$ Å, $c = 9.502$ Å) [11]. Lattice parameters and local geometrical parameters of the undoped TiO_2 and doped TiO_2 supercells are presented in Table I. The lattice constants ($a = 11.417$ Å, $c = 9.723$ Å) of the undoped anatase TiO_2 were in good consonance with the lattice constants obtained from experiments ($3 \times a = 11.346$ Å, $c = 9.502$ Å) [11], with a structural deviation of 2–3 %. The lateral lattice constants (a and b) were slightly higher for the doped anatase TiO_2 compared with the undoped case. In contrast, the perpendicular lattice constant (c) was slightly lower for the doped anatase TiO_2. Furthermore, we found that there was minute modulation in the M-O

TABLE I. Lattice parameters of the undoped and doped anatase TiO_2 supercell, M-O, Ti-O, and Ti-F bond lengths at the doping position obtained using the PBE functional.

	a (Å)	c (Å)	Ti-O_1 (Å)	Ti-O_2 (Å)	Ti-O_3 (Å)	Ti-O_4 (Å)	Ti-O_5 (Å)	Ti-O_6 (Å)
TiO_2 expt.[a]		9.502	1.934	1.934	1.934	1.934	1.980	1.980
TiO_2	11.417	9.723	1.950	1.950	1.950	1.950	2.007	2.007
	a (Å)	c (Å)	M-O_1 (Å)	M-O_2 (Å)	M-O_3 (Å)	M-O_4 (Å)	M-O_5 (Å)	M-O_6 (Å)
TiO_2:V	11.422	9.699	1.940	1.940	1.940	1.940	1.912	1.912
TiO_2:Cr	11.417	9.699	1.927	1.927	1.927	1.927	1.917	1.917
TiO_2:Nb	11.445	9.718	1.978	1.978	1.978	1.978	2.049	2.049
TiO_2:Mo	11.446	9.693	1.950	1.950	1.950	1.950	1.957	1.957
TiO_2:Ta	11.444	9.715	1.968	1.968	1.968	1.968	2.027	2.027
TiO_2:W	11.461	9.675	1.922	1.922	1.922	1.922	1.964	1.964
	a (Å)	c (Å)	Ti-O_1 (Å)	Ti-O_2 (Å)	Ti-O_3 (Å)	Ti-O_4 (Å)	Ti-O_5 (Å)	Ti-F (Å)
TiO_2:F	11.450	9.689	1.960	1.940	1.960	1.940	1.874	2.245

[a]To compare with the supercell, only the lattice parameter of c-axis and Ti-O bond lengths were taken from Ref. [11].

distances, indicating a slight structural distortion. In the case of TiO_2:M, the equatorial bond lengths (M-O_1, M-O_2, M-O_3, M-O_4) and apical bond lengths (M-O_5, M-O_6) were fixed; M-$O_1 = M$-$O_2 = M$-$O_3 = M$-O_4, M-$O_5 = M$-O_6. In contrast, for the TiO_2:F case, the O_6-atom was replaced by atom F [Fig. 1(d)], which resulted in the change of the bond lengths; Ti-O_1 = Ti-O_3 ≠ Ti-O_2 = Ti-O_4, Ti-O_5 ≠ Ti-F.

Figure 2 shows the unfolded band structures of the undoped anatase TiO_2, TiO_2:M, and TiO_2:F. The undoped anatase TiO_2 was found to be a semiconductor with an indirect band gap of ∼2.1 eV, where the conduction-band minimum (CBM) was located in the Γ point and the valence-band maximum (VBM) was located between Γ and X, as shown in Fig. 2(a). The band gaps were underestimated compared

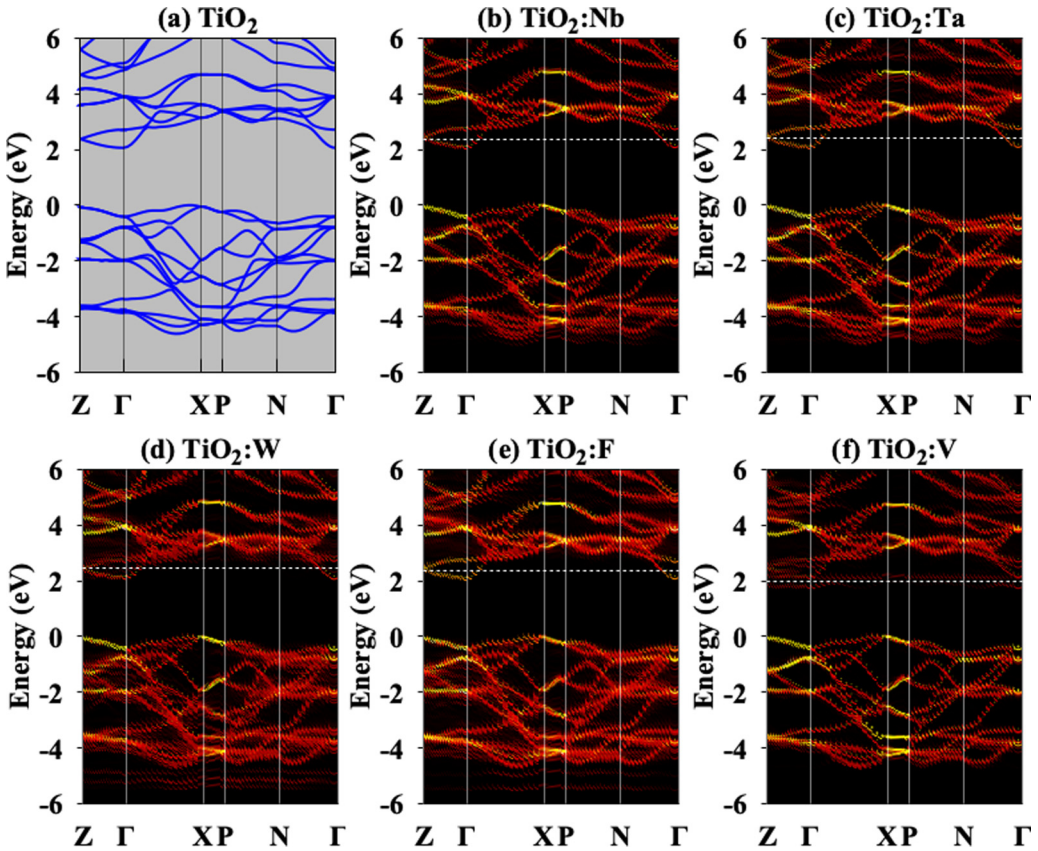

FIG. 2. (a) Electronic band structure of anatase TiO_2 primitive cell; unfolded band structures of the 108-atom supercells (b) TiO_2:Nb, (c) TiO_2:Ta, (d) TiO_2:W, (e) TiO_2:F, and (f) TiO_2:V spin-up. The horizontal dashed lines indicate positions of the Fermi levels (E_F). The top of the valence band of the undoped anatase TiO_2 was set at 0 eV as a reference. Results for the spin-down channel of TiO_2:V, unfolded band structures of TiO_2:Cr, and TiO_2:Mo are reported in the supplemental material (Figs. S3–S5).

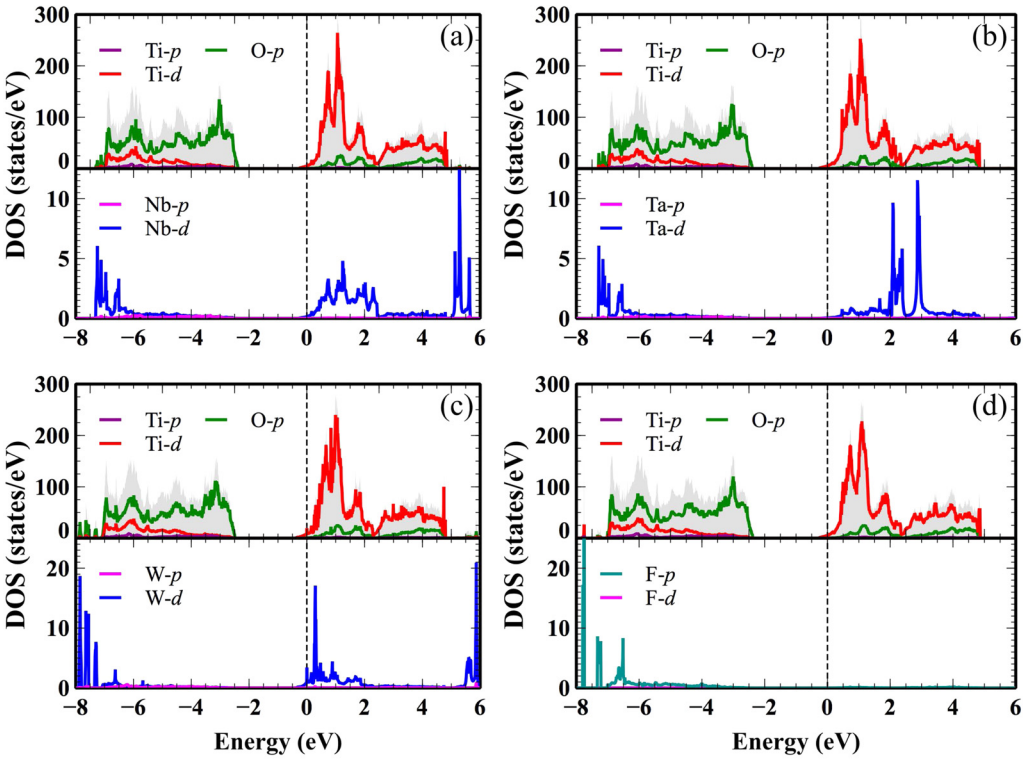

FIG. 3. Atomic orbital projected DOS (states/eV) of (a) TiO_2:Nb, (b) TiO_2:Ta, (c) TiO_2:W, and (d) TiO_2:F. The vertical dashed lines indicate the position of the Fermi level at 0 eV. The gray shadows represent the total DOS.

with the band gap obtained from experiments (3.2 eV) [45] because of the GGA-PBE exchange-correlation functional used in this work. We checked the energy band gap using the more accurate HSE06 hybrid functional based on the relaxed structures and magnetic ordering determined using the PBE functional, and we found that the band gap was 3.54 eV, which showed good agreement with the one from experiments (3.2 eV), as shown in Fig. S1 of the Supplemental Material.

The electron effective mass of the primitive cell of anatase TiO_2 crystal was estimated from the band structure [Fig. 2(a)] by the second derivative of energy band $E(\mathbf{k})$. In the parallel direction (Γ-Z) to the tetragonal axis, the effective mass ($4.22m_0$)) is significantly larger than those in the orthogonal direction (Γ-X) ($0.43m_0$), where m_0 is the free-electron mass. These effective-mass values are consistent with previous studies ($4.05m_0$ and $0.42m_0$ in the parallel and orthogonal direction, respectively) [57,58].

The Nb-, Ta-, W-, and F-doped anatase TiO_2 crystals presented metallic behavior, where the Fermi levels were located within the conduction bands of anatase TiO_2 crystal [Figs. 2(b)–2(e)]. Interestingly, comparing the band dispersion between the doped and undoped anatase TiO_2 crystals, it was evident that the valence and conduction bands of the doped anatase TiO_2 crystals are similar to those of undoped counterparts. Furthermore, based on the projected density of states [Figs. 3(a)–3(d)], there was negligible modulation of the DOS for the Ti and O atoms in the doped TiO_2 crystals compared with that for the Ti and O atoms in the undoped TiO_2 crystal. The results indicated that the Nb, Ta, W, and F dopants acted as physical donors, and the excessive electrons of these dopant atoms (compared with the Ti and O atoms) were physically transferred to the TiO_2 lattice, resulting in n-type doped TiO_2 [59,60].

The TiO_2:V, TiO_2:Cr, and TiO_2:Mo crystals exhibited magnetic properties with a magnetic moment of 0.77 μ_B/V atom, 1.89 μ_B/Cr atom, and 0.58 μ_B/Mo atom, respectively. Because of magnetic properties, band structures for TiO_2:V [Fig. 2(f) and Fig. S3], TiO_2:Cr (Fig. S4), and TiO_2:Mo (Fig. S5) were separated into two parts: spin up and spin down. In addition, the conduction bands of these doped TiO_2 crystals appeared as new flat bands near the Fermi levels. We clarified that these new flat bands were the localized $3d$- or $4d$-electrons of the V, Cr, or Mo atoms based on the projected density of states (Figs. S3–S5 of the supplemental material). Therefore, it could be expected that optical properties of TiO_2:V, TiO_2:Cr, and TiO_2:Mo would be different from those of TiO_2:Nb, TiO_2:Ta, TiO_2:W, and TiO_2:F. Here, we focused on the optical properties of TiO_2-based TCOs, which exhibited prototype metallic properties without significant modulations in the TiO_2 electronic structure near the Fermi level. Thus, we would only discuss the electronic and optical properties of anatase TiO_2 crystals doped with nonmagnetic dopants (Nb, Ta, W, and F) in the following section, which clearly presented n-type doping and metallic feature.

Figure 3 shows the projected DOS of the Nb-, Ta-, W-, and F-doped anatase TiO_2. Only p and d states were presented here because the contributions of s states are very small. It is obvious that all compounds have similar total DOS. The valence band is mainly formed from the O p states. There is no impurity-induced gap state within the band gap, indicating

TABLE II. Carrier concentration (n_e), DOS effective mass (m^*), estimated plasma frequency (ω_p) at the Fermi level E_F (for DOS calculations), plasma frequencies ($\omega_p^{\perp}$, $\omega_p^{\parallel}$), and crossover frequencies ($\omega_c^{\perp}$, $\omega_c^{\parallel}$) of the doped anatase TiO_2 crystals perpendicular and parallel to the c-axis, respectively.

	TiO_2:Nb	TiO_2:Ta	TiO_2:W	TiO_2:F
$n_e(10^{21}\,\mathrm{cm}^{-3})$	0.77	0.78	1.57	0.79
m^* at E_F	1.07	1.10	1.24	1.11
ω_p at E_F (eV)	1.00	0.99	1.31	0.99
$\omega_p^{\perp}$ (eV)	1.32	1.31	1.47	1.27
$\omega_p^{\parallel}$ (eV)	0.36	0.37	0.28	0.38
$\omega_c^{\perp}$ (μm)	2.62	2.62	2.02	2.74
$\omega_c^{\parallel}$ (μm)	11.15	10.84	37.80	10.62

that the compounds have high optical transparency in the visible region [13].

Because of the anisotropic geometry of anatase TiO_2, the optical properties were dependent on their orientation. For a tetragonal structure ($a = b$, $c \neq a$), the complex dielectric functions of the doped anatase TiO_2 could be separated into the following parts: (i) $\varepsilon^{\perp} = \varepsilon_{xx} = \varepsilon_{yy}$ ($\mathbf{E} \perp c$, perpendicular to the c-axis) and (ii) $\varepsilon^{\parallel} = \varepsilon_{zz}$ ($\mathbf{E} \parallel c$, parallel to the c-axis).

We estimated the carrier concentration and DOS effective mass of the doped anatase TiO_2 crystals, which are the essential parameters for plasmonic applications. The anatase TiO_2 crystal became a metallic system through the doping, and therefore it is necessary to discuss the DOS effective mass at the Fermi level. We found that the DOS effective mass at the Fermi level of TiO_2:W ($1.24m_0$) is higher than that of TiO_2:M (M = Nb,Ta,F) ($\sim 1.07m_0$), indicating that TiO_2:W could have lower electron mobility than TiO_2:M (M = Nb,Ta,F). The procedure used to calculate the carrier concentration is described in detail in the supplemental material [Sec. S3(a)]. The carrier concentrations of the Nb-, Ta-, W-, and F-doped anatase TiO_2 crystals at absolute zero temperature are presented in Table II. Note that compensation with hole carriers induced by native defects such as oxygen interstitials or Ti vacancies is ignored in these estimations. This is a good approximation because TiO_2 is known as an n-type semiconductor, and the intrinsic carrier density is much lower [56] than that discussed in the following. We found that the carrier concentrations of TiO_2:Nb, TiO_2:Ta, and TiO_2:F were 0.77×10^{21}, 0.78×10^{21}, and $0.79 \times 10^{21}\,\mathrm{cm}^{-3}$, respectively. In these doped anatase TiO_2 crystals, the Nb, Ta, and F atoms donate one electron to the TiO_2 lattice. The TiO_2:W has a higher carrier concentration of $1.57 \times 10^{21}\,\mathrm{cm}^{-3}$ because this dopant has two excessive valence electrons compared with the Ti atom and can donate two electrons.

Next, we studied the optical properties of the doped anatase TiO_2 to assess their potential for optoelectronic devices. The performance of plasmonic materials depends mainly on their structures and physical properties. Figures 4(a) and 4(b) show the real and imaginary parts of the dielectric functions of TiO_2:Nb, TiO_2:Ta, TiO_2:W, and TiO_2:F.

Although the simulation with the HSE06 hybrid exchange-correlation functional provided a more accurate estimation of the band gap than the PBE functional, simulations with the HSE06 functional did not significantly alter the band dispersion of the valence and conduction states of the doped anatase TiO_2 (Fig. S2 of the supplemental material). Also, the *GW* approximation gives more accurate results for the optical transitions, but because of the large size of these systems it is impossible to apply the *GW* approximation in this study to obtain a sufficiently accurate result. Our focus is on infrared applications; therefore, we focus mainly on the low-energy intraband region of the optical response, which corresponds to an energy region smaller than 1.6 eV. Several references show that there were no significant differences between the dielectric functions of anatase using the *GW* approximation and the PBE compared to experiments in the low-energy limit below 1.6 eV [61,62]. Furthermore, we applied the Drude model to calculate the intraband dielectric function. The Drude model is considerably dependent on plasma frequency, which can be estimated from the shape of the valence bands and conduction bands rather than the band gap. Several studies used HSE06 or *GW* to improve the accuracy of energy bands of anatase TiO_2, but the shape of the valence bands and conduction bands does not change significantly [61,63,64]. For doped semiconductor systems in this study, which show metallic behavior, the two components that contribute to the total dielectric function are interband and intraband transitions. We admit that substantial

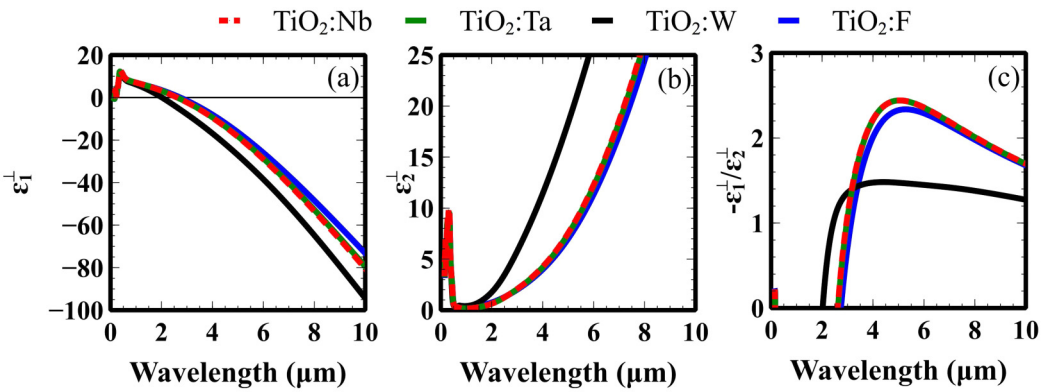

FIG. 4. Calculated (a) real parts and (b) imaginary parts of the total dielectric functions (interband and intraband electron transitions). (c) Figure of merit (FOM) of the doped anatase TiO_2 crystals along the direction perpendicular to the c-axis. The curves of the dielectric functions for TiO_2:Nb (red) and TiO_2:Ta (green) overlap each other.

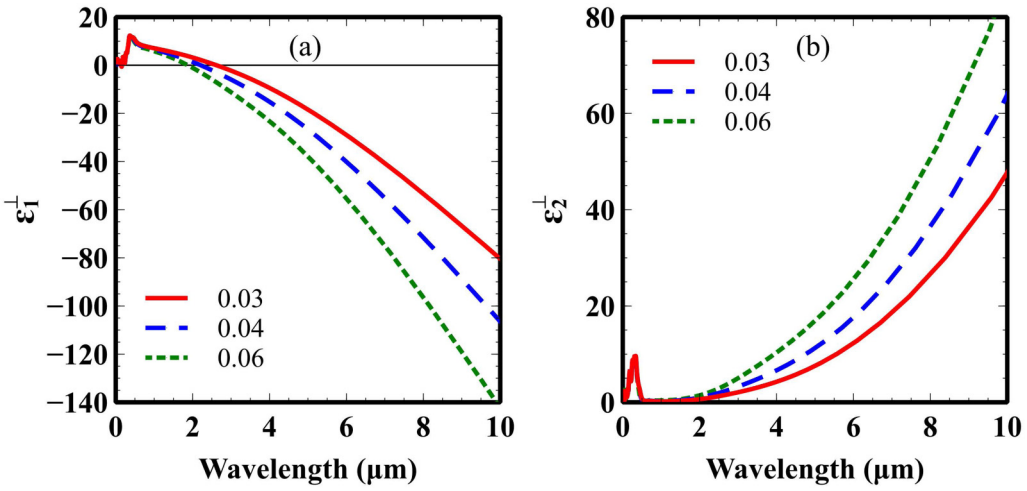

FIG. 5. Calculated (a) real permittivity, (b) imaginary permittivity of the doped anatase $Ti_{1-x}Nb_xO_2$ systems ($x = 0.03,0.04,0.06$) perpendicular to the c-axis.

error exists for interband transitions in the visible region, but we consider that there is no significant difference between the intraband dielectric functions using the PBE functional and the HSE06/*GW* approximation in the low-energy limit. Namely, we can state that different simulation methods show little effect on optical properties in the low-energy midinfrared region. For example, the PBE functional with the IPA model can be safely used to investigate optical properties in the infrared region. Also, since real experimental systems are affected by many other factors such as crystallinity and surface roughness, the current approach with the IPA model can be used to assess the optical properties in the infrared region. Recently, we succeeded in synthesizing high-quality doped TiO_2 films, and we found that the agreement in the midinfrared region is satisfactorily good [65].

Here, we focused on the optical properties of the doped anatase TiO_2 along the highest plasma frequency direction (perpendicular to the c-axis). The most important quantity, which should be taken into account here, is the crossover frequency (or screened plasma frequency), defined as the frequency (wavelength) where the real part of the dielectric function crosses the zero value. We found that the crossover frequency was within a range of 2.0–2.7 μm for the Nb-, Ta-, W-, and F-doped anatase TiO_2 indicating their suitability for IR photonic applications. The results on the total dielectric functions clearly show that Nb, Ta, and F exhibit nearly the same optical properties. Since fabrication of F-doped TiO_2 requires special chemical treatment, and the price of each metric ton of tantalum is about \$140 000, but that of niobium is only about \$42 000 [66], it is more desirable to select a low-cost and more stable dopant such as Nb for practical applications with large-scale IR plasmonic devices.

Figure 4(c) shows the figure of merit (FOM) defined by the ratio between the real permittivity and the imaginary permittivity of TiO_2:Nb, TiO_2:Ta, TiO_2:W, and TiO_2:F, which can value the quality factor and near-field enhancement of the LSPR. It could be seen that Nb-, Ta-, and F-doped anatase TiO_2 had superior performance compared to the W-doped anatase TiO_2 because of their low-loss nature. The FOM values were greater than 1 in the IR region for all curves. This proves that the Nb-, Ta-, W-, and F-doped anatase TiO_2 are highly promising materials for IR LSPR applications. For most transformation optics (TO) devices, the smaller the imaginary part of the total dielectric function, the better is the material. The Nb-, Ta-, and F-doped anatase TiO_2 has better performance than the W-doped TiO_2 for TO devices, which can be attributed to the higher loss of TiO_2:W compared with those of TiO_2:Nb, TiO_2:Ta, and TiO_2:F.

In general, plasma frequency is strongly dependent on dopant concentration. To demonstrate the potential of doped semiconductors as tunable plasmonic materials, we constructed three models to investigate the plasma frequency and carrier density of doped semiconductors as a function of the dopant concentration (Fig. 5 and Table III). The dopant concentrations (x), which correspond to the 108-, 72-, and 48-atom supercells, were 0.03, 0.04, and 0.06, respectively. We chose these particular dopant concentrations because $0.03 \leqslant x \leqslant 0.06$ was the optimum range of dopant concentrations in experiments, resulting in high electrical conductivity and optical transmittance [13].

As seen in Table III, the plasma frequency $\omega_p^\perp$ along the highest plasma frequency direction ($\perp c$) increases with the increase of the dopant concentration x following the expression $\omega_p = (\frac{n_e e^2}{\varepsilon_0 m^*})^{\frac{1}{2}}$ [see the Supplemental Material, Sec. S3(c)],

TABLE III. Carrier concentration (n_e), plasma frequency ($\omega_p^\perp$), and crossover frequency (ω_c) for different Nb concentrations x along the highest plasma frequency direction ($\perp c$).

x	Supercell	n_e (10^{21} cm^{-3})	$\omega_p^\perp$ (eV)	$\omega_c^\perp$ (μm)
0.03	3 × 3 × 1	0.77 (∼0.7)[a]	1.32	2.62
0.04	3 × 2 × 1	1.14 (∼1.2)[a]	1.51	2.22
0.06	2 × 2 × 1	1.76 (∼1.7)[a]	1.74	1.88

[a]Data extracted from Ref. [13].

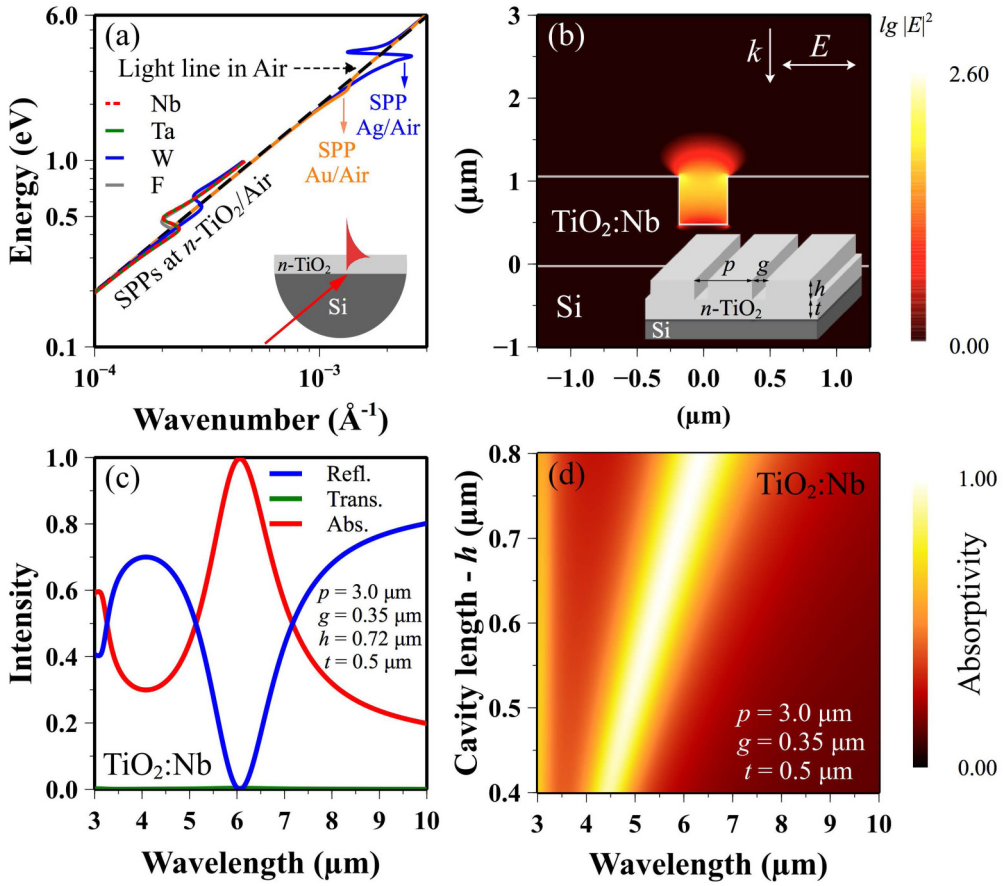

FIG. 6. (a) Calculated SPPs dispersion curves at the noble metals (Au,Ag)/air and n-type doped anatase TiO_2/air interfaces. The inset shows attenuated total reflection (ATR) geometry for SPP excitation. (b) Simulated electric field distribution of an IR plasmonic TiO_2:Nb nanocavity array excited at the resonant wavelength of 6 μm. The inset in (b) shows the proposed structural geometry. (c) Simulated reflectance, transmittance, and absorptivity of a TiO_2:Nb periodic cavity array working as a plasmonic antenna for SEIRA. (d) The tunability of the plasmon resonance in the mid-IR region demostrated for the TiO_2:Nb cavity array (the cavity length $h = 0.4 - 0.8\mu$m).

which also agrees well with the experimental results reported previously [13].

B. Electromagnetic simulations of plasmonic n-type doped anatase TiO_2 structures

Recently, ITO and other TCOs have proven to be the materials of choice to study surface plasmons in the mid-IR region because they exhibited screened plasma frequencies in this region [5,32,33,67,68]. To demonstrate the plasmonic properties of n-type doped anatase TiO_2 films, we first studied the SPPs on the surface of n-type doped anatase TiO_2 thin films. In this work, we used the Kretschmann configuration supported by an attenuated total reflection (ATR) Si hemi-cylindrical prism [inset in Fig. 6(a)] to analytically investigate the SPPs of the n-type doped anatase TiO_2 thin films. Figure 6(a) shows the calculated SPP dispersion curves at the n-type doped anatase TiO_2 film/air interface. The SPP dispersion curves at the noble metal (Au, Ag)/air interfaces were also plotted for comparison. The dispersion curves indicate that the SPPs of the n-type doped TiO_2 films/air reside in the low-energy region (IR region). Interestingly, compared to the noble metal films, the n-type doped anatase TiO_2 films exhibit SPPs in the mid-IR region (below 0.5 eV) whereas noble metals behave as perfect electrical conductors in this region. This proves that the n-type doped anatase TiO_2 films are favorable candidates to study SPPs in the IR region, similar to other plasmonic TCO materials [69].

Nowadays there is much interest in the use of plasmonic ITOs among plasmonic oxide nanoantennas for surface-enhanced infrared absorption spectroscopy (SEIRA) [70–72] applications due to the advantages of their oxide surface functionalization [34,73] and tunability of the IR screened plasma frequencies. Figure 6(b) shows the simulated electric field intensity distribution of a plasmonic TiO_2:Nb nanocavity array at a resonance excitation of 6 μm. The plasmonic structure showed a strong electric field enhancement confined within the vertical cavity at the resonant excitation, indicating that the TiO_2:Nb cavity array is a good candidate for SEIRA applications. The inset in Fig. 6(b) shows the structural geometry of the TiO_2:Nb nanocavity array with a periodicity p, cavity gap g, length h, and bottom film thickness t. For example, a perfect resonance absorption of 6 μm targeted at an amide I vibrational band can be realized by fabricating a plasmonic TiO_2:Nb nanocavity array with the following geometrical parameters: $p = 3$, $g = 0.35$, $h = 0.72$, and $t = 0.5$ μm [Fig. 6(c)]. By simply varying the cavity length h from 0.4 to 0.8 μm [Fig. 6(d)] while keeping the other parameters

constant ($p = 3$, $g = 0.35$, and $t = 0.5\ \mu$m), the resonance of the plasmonic cavity array is tunable in the mid-IR region and covers the most important molecular vibrations (e.g., C = O, amide I, and amide II bands). With strong near-field intensity enhancement (e.g., ∼400 times) at the plasmonic cavity, high absorptivity, low loss, and feasible tunability, the plasmonic TiO_2:Nb nanocavity array proposed in this work can also be applied in other IR plasmonic devices such as thermal emitters or visible-transparent IR selective absorbers for smart windows.

IV. CONCLUSIONS

In this work, we investigated the effects of doping based on six transition metals from group V-B (V, Nb, Ta) and group VI-B (Cr, Mo, W) and an element from group VII-A (F) on the electronic structures and optical properties of anatase TiO_2 using first-principles DFT and the IPA model. Based on the electronic band structures of undoped and doped anatase TiO_2, we showed that the dopants Nb, Ta, W, and F preserved the natural structural properties of anatase TiO_2 while showing strong metallic behavior close to the nearly-free-electron system. The optical properties of Nb-, Ta-, W-, and F-doped anatase TiO_2 were analyzed, and their performances in the IR region were compared. We concluded that Nb-, Ta-, W-, and F-doped anatase TiO_2 are promising candidates for IR plasmonic applications, with a crossover frequency within a range of 2.0–2.7 μm. As a proof of concept, SPPs and LSPR resonances of the doped anatase TiO_2 were examined by using analytical and numerical simulations. The simulated results evidenced that doped TiO_2 can be a good plasmonic material platform for IR plasmonic devices such as for SEIRA and IR emitters. The results obtained here will be useful for further exploration of practical IR plasmonic materials based on various oxide semiconductors.

ACKNOWLEDGMENTS

This work is partially supported by JSPS KAKENHI (16F16315, JP16H06364, 16H03820) and CREST "Phase Interface Science for Highly Efficient Energy Utilization" (JPMJCR13C3) from Japan Science and Technology Agency. The authors wish to thank Mukesh Kumar and Hai Dang Ngo for their helpful discussions. The simulations in this study were performed using the Numerical Materials Simulator at NIMS and partially supported by the Supercomputer System at the Information Initiative Center, Hokkaido University.

The authors declare no conflict of interest.

[1] C. Kittel, *Introduction to Solid State Physics*, 8th ed. (John Wiley & Sons, 2004).
[2] H. Watanabe, J. Phys. Soc. Jpn. **11**, 112 (1956).
[3] H. Raether, *Surface Plasmons on Smooth and Rough Surfaces and on Gratings* (Springer, Berlin, 1988).
[4] P. R. West, S. Ishii, G. V. Naik, N. K. Emani, V. M. Shalaev, and A. Boltasseva, Laser Photon. Rev. **4**, 795 (2010).
[5] S. Franzen, J. Phys. Chem. C **112**, 6027 (2008).
[6] G. V. Naik and A. Boltasseva, Phys. Status Solidi–Rapid Res. Lett. **4**, 295 (2010).
[7] https://www.pilkington.com/en-gb/uk/householders/types-of-glass/energy-efficient-glass.
[8] H. Sasabe and J. Kido, J. Mater. Chem. C **1**, 1699 (2013).
[9] P. Spathis and I. Poulios, Corros. Sci. **37**, 673 (1995).
[10] A. Fujishima and K. Honda, Nature (London) **238**, 37 (1972).
[11] J. K. Burdett, T. Hughbanks, G. J. Miller, J. W. Richardson, and J. V. Smith, J. Am. Chem. Soc. **109**, 3639 (1987).
[12] T. Yamamoto and T. Ohno, Phys. Rev. B **85**, 033104 (2012).
[13] T. Hitosugi, N. Yamada, S. Nakao, Y. Hirose, and T. Hasegawa, Phys. Status Solidi **207**, 1529 (2010).
[14] Y. Furubayashi, T. Hitosugi, Y. Yamamoto, K. Inaba, G. Kinoda, Y. Hirose, T. Shimada, and T. Hasegawa, Appl. Phys. Lett. **86**, 252101 (2005).
[15] S. Mohri, Y. Hirose, S. Nakao, N. Yamada, T. Shimada, and T. Hasegawa, J. Appl. Phys. **111**, 093528 (2012).
[16] U. Takeuchi, A. Chikamatsu, T. Hitosugi, H. Kumigashira, M. Oshima, Y. Hirose, T. Shimada, and T. Hasegawa, J. Appl. Phys. **107**, 023705 (2010).
[17] M. Bernardi, J. Mustafa, J. B. Neaton, and S. G. Louie, Nat. Commun. **6**, 7044 (2015).
[18] Z. Tong, S. Li, X. Ruan, and H. Bao, Phys. Rev. B **100**, 144306 (2019).
[19] J. I. Mustafa, M. Bernardi, J. B. Neaton, and S. G. Louie, Phys. Rev. B **94**, 155105 (2016).
[20] A. M. Brown, R. Sundararaman, P. Narang, W. A. Goddard, and H. A. Atwater, Phys. Rev. B **94**, 075120 (2016).
[21] T. Gunst, T. Markussen, K. Stokbro, and M. Brandbyge, Phys. Rev. B **93**, 035414 (2016).
[22] A. Habib, F. Florio, and R. Sundararaman, J. Opt. **20**, 064001 (2018).
[23] J. Kim, S.-H. Jhi, and K. Ryeol Lee, J. Appl. Phys. **110**, 083501 (2011).
[24] K. Glantschnig and C. Ambrosch-Draxl, New J. Phys. **12**, 103048 (2010).
[25] S. Laref, J. Cao, A. Asaduzzaman, K. Runge, P. Deymier, R. W. Ziolkowski, M. Miyawaki, and K. Muralidharan, Opt. Express **21**, 11827 (2013).
[26] M. Kumar, N. Umezawa, S. Ishii, and T. Nagao, ACS Photon. **3**, 43 (2016).
[27] M. Kumar, S. Ishii, N. Umezawa, and T. Nagao, Opt. Mater. Express **6**, 29 (2016).
[28] G. Prandini, G.-M. Rignanese, and N. Marzari, npj Comput. Mater. **5**, 129 (2019).
[29] Y. Furubayashi, N. Yamada, Y. Hirose, Y. Yamamoto, M. Otani, T. Hitosugi, T. Shimada, and T. Hasegawa, J. Appl. Phys. **101**, 093705 (2007).
[30] L. Thulin and J. Guerra, Phys. Rev. B **77**, 195112 (2008).
[31] T. D. Dao, A. T. Doan, D. H. Ngo, K. Chen, S. Ishii, A. Tamanai, and T. Nagao, Opt. Mater. Express **9**, 2534 (2019).
[32] M. Kanehara, H. Koike, T. Yoshinaga, and T. Teranishi, J. Am. Chem. Soc. **131**, 17736 (2009).
[33] S. Q. Li, P. Guo, L. Zhang, W. Zhou, T. W. Odom, T. Seideman, J. B. Ketterson, and R. P. H. Chang, ACS Nano **5**, 9161 (2011).

[34] K. Chen, P. Guo, T. D. Dao, S. Q. Li, S. Ishiii, T. Nagao, and R. P. H. Chang, Adv. Opt. Mater. **5**, 1700091 (2017).

[35] P. Guo, R. D. Schaller, J. B. Ketterson, and R. P. H. Chang, Nat. Photon. **10**, 267 (2016).

[36] X. Liu, J.-H. Kang, H. Yuan, J. Park, S. J. Kim, Y. Cui, H. Y. Hwang, and M. L. Brongersma, Nat. Nanotechnol. **12**, 866 (2017).

[37] P. E. Blöchl, Phys. Rev. B **50**, 17953 (1994).

[38] G. Kresse and J. Furthmüller, Comput. Mater. Sci. **6**, 15 (1996).

[39] J. P. Perdew, K. Burke, and M. Ernzerhof, Phys. Rev. Lett. **77**, 3865 (1996).

[40] J. D. Pack and H. J. Monkhorst, Phys. Rev. B **16**, 1748 (1977).

[41] V. Popescu and A. Zunger, Phys. Rev. B **85**, 085201 (2012).

[42] P. V. C. Medeiros, S. Stafström, and J. Björk, Phys. Rev. B **89**, 041407 (2014).

[43] P. V. C. Medeiros, S. S. Tsirkin, S. Stafström, and J. Björk, Phys. Rev. B **91**, 041116 (2015).

[44] J. Heyd, G. E. Scuseria, and M. Ernzerhof, J. Chem. Phys. **124**, 219906 (2006).

[45] S. P. Kowalczyk, F. R. McFeely, L. Ley, V. T. Gritsyna, and D. A. Shirley, Solid State Commun. **23**, 161 (1977).

[46] M. Gajdoš, K. Hummer, G. Kresse, J. Furthmüller, and F. Bechstedt, Phys. Rev. B **73**, 045112 (2006).

[47] See Supplemental Material at http://link.aps.org/supplemental/10.1103/PhysRevMaterials.4.055201 for the dielectric functions along the *zz*-component ($E \parallel c$).

[48] H. Ehrenreich and H. R. Philipp, Phys. Rev. **128**, 1622 (1962).

[49] F. Wooten, *Optical Properties of Solids* (Academic Press, New York, 1972).

[50] J. Harl, The linear response function in density functional theory: Optical spectra and improved description of the electron correlation, Ph.D. thesis, University of Vienna, 2008.

[51] M. P. Desjarlais, J. D. Kress, and L. A. Collins, Phys. Rev. E **66**, 025401 (2002).

[52] R. Kubo, J. Phys. Soc. Jpn. **12**, 570 (1957).

[53] L. L. Moseley and T. Lukes, Am. J. Phys. **46**, 676 (1978).

[54] M. Dressel and G. Gruener, *Electrodynamics of Solids: Optical Properties of Electrons in Matter* (Cambridge University Press, Cambridge, 2002).

[55] K. Momma and F. Izumi, J. Appl. Crystallogr. **44**, 1272 (2011).

[56] A. Boonchun, P. Reunchan, and N. Umezawa, Phys. Chem. Chem. Phys. **18**, 30040 (2016).

[57] Y. Hirose, N. Yamada, S. Nakao, T. Hitosugi, T. Shimada, and T. Hasegawa, Phys. Rev. B **79**, 165108 (2009).

[58] H. Kamisaka, T. Hitosugi, T. Suenaga, T. Hasegawa, and K. Yamashita, J. Chem. Phys. **131**, 034702 (2009).

[59] J. Biedrzycki, S. Livraghi, E. Giamello, S. Agnoli, and G. Granozzi, J. Phys. Chem. C **118**, 8462 (2014).

[60] S. Sathasivam, D. S. Bhachu, Y. Lu, N. Chadwick, S. A. Althabaiti, A. O. Alyoubi, S. N. Basahel, C. J. Carmalt, and I. P. Parkin, Sci. Rep. **5**, 10952 (2015).

[61] C. E. Patrick and F. Giustino, J. Phys. Condens. Matter **24**, 202201 (2012).

[62] H. Ünal, O. Gülseren, S. Ellialtioglu, and E. Mete, Phys. Rev. B **89**, 205127 (2014).

[63] M. Landmann, E. Rauls, and W. G. Schmidt, J. Phys. Condens. Matter **24**, 195503 (2012).

[64] L. Chiodo, J. M. García-Lastra, A. Iacomino, S. Ossicini, J. Zhao, H. Petek, and A. Rubio, Phys. Rev. B **82**, 045207 (2010).

[65] H. D. Ngo, K. Chen, O. S. Handegard, A. T. Doan, T. D. Ngo, T. D. Dao, N. Ikeda, A. Ohi, T. Nabatame, and T. Nagao, Micromachines **11**, 23 (2019).

[66] https://www.metalary.com/.

[67] P. F. Robusto and R. Braunstein, Phys. Status Solidi **119**, 155 (1990).

[68] C. Rhodes, S. Franzen, J.-P. Maria, M. Losego, D. N. Leonard, B. Laughlin, G. Duscher, and S. Weibel, J. Appl. Phys. **100**, 054905 (2006).

[69] A. Tamanai, T. D. Dao, M. Sendner, T. Nagao, and A. Pucci, Phys. Status Solidi **214**, 1600467 (2017).

[70] F. Neubrech, A. Pucci, T. W. Cornelius, S. Karim, A. García-Etxarri, and J. Aizpurua, Phys. Rev. Lett. **101**, 157403 (2008).

[71] D. Enders, T. Nagao, A. Pucci, T. Nakayama, and M. Aono, Phys. Chem. Chem. Phys. **13**, 4935 (2011).

[72] C. V. Hoang, M. Oyama, O. Saito, M. Aono, and T. Nagao, Sci. Rep. **3**, 1175 (2013).

[73] K. Chen, T. D. Dao, S. Ishii, M. Aono, and T. Nagao, Adv. Funct. Mater. **25**, 6637 (2015).